A Contextual and Multitemporal Active-Fire Detection Algorithm Based on FengYun-2G S-VISSR Data

Zhengyang Lin, Fang Chen, Bin Li, Bo Yu, Huicong Jia, Meimei Zhang, and Dong Liang

***Abstract*— Wildfires are one of the most destructive disasters on the planet. They also significantly impact the land surface. Satellite data have been widely used to detect the outbreak and monitor the expansion of fire incidents for damage assessment and disaster management. Polar-orbiting satellite data have been used for several decades but data from geostationary satellites, which can provide observations with a high temporal resolution, have received much less attention. This paper utilizes data from FengYun-2G, a Chinese geostationary satellite, to detect wildfires in two selected research regions in January 2016. The detection algorithm systemizes image-based analysis to filter out obvious nonfire pixels and temporal analysis to confirm the true detections. Fire detection is based on comparisons between predicted and observed values. The results show that the proposed method has some advantages compared with the use of polar-orbiting satellite data, including early detection and continuous observation. The validation work is conducted based on the collection 6.1 Global Monthly Fire Location Product generated from fire detections by Moderate Resolution Imaging Spectroradiometer (MODIS) sensors. The average accuracy within the target time is 56%, while the omission error rate is over 78%. In detail, the algorithm has a lower omission error rate in Australia while it fails in detecting most of the fire pixels in India. The dominance of small fire incidents, as well as low spatial resolution greatly limit the detection ability. Many small fires were beyond the ability of Stretched Visible and Infrared Spin Scan Radiometer (S-VISSR) data when no significant fire characteristics could be captured. Future development of the algorithm will focus on improving the results by enhancing the adaption to different regions, as well as, including multisource data sets.**

***Index Terms*— Active fire detection algorithm, FengYun-2G, geostationary satellite data.**

I. Introduction

WILDFIRES have heavily influenced both natural and artificial environments [1]–[4]. The biomass burning caused by wildfires is one of the major factors that cause changes in land surfaces [5]. Some researchers have estimated that the total annual area burned globally is as high as 6×106 ha [6].

The detection and monitoring of wildfires have always been challenging. Satellites carrying instruments with mid-infrared and thermal infrared channels can provide researchers and decision-makers with a general view of fires within short time periods. Therefore, analyzing the relevant satellite data has become an important problem that needs to be solved.

Research in this field began when Matson and Dozier [7] used data from the NOAA Advanced Very High-Resolution Radiometer (AVHRR) to detect active fires. In the following decades, numerous algorithms and fire products were generated. Dozier [8] used AVHRR data to build a model that revealed the relationship between a fire pixel and its internal subpixels. This model became the theoretical basis for further fire-detection work. Flannigan and Vonderhaar [9] applied the threshold method, while Lee and Tag [10] developed the contextual method for the detection of active burning pixels. Giglio *et al.* [11] designed an enhanced contextual algorithm, which combined the absolute threshold, the contextual method, and false alarm elimination and was based on Moderate Resolution Imaging Spectroradiometer (MODIS) data. The ideas behind the enhanced contextual algorithm have proved to be effective in various environments and for many different types of data. Much of the subsequent research that has been carried out has been based on this algorithm. Giglio *et al.* [12] upgraded the algorithm to version 6, which was able to detect fires in water areas, while Csiszar *et al.* [13] and Schroeder *et al.* [14] applied it to the Visible Infrared Imaging Radiometer Suite (VIIRS). Lin *et al.* [15] achieved improved results by applying the contextual algorithm to Visible and Infra-Red Radiometer (VIRR) from FengYun-3C, a Chinese meteorological polar-orbiting satellite. In addition, much other research has been done to improve the performance of active fire detection algorithms using different data sets [16]–[25].

While geostationary satellites can provide users with high-temporal resolution images, which is very important in detecting rapid changes, such as wildfire incidents, the low spatial resolution and lack of appropriate algorithms has hindered the application of these data [26]–[35]. One of the earliest studies that attempted to examine the ability of geostationary satellites to detect biomass burning was carried out by Prins and Menzel [36] using Geostationary Operational Environmental Satellite (GOES) data. Roberts and Wooster [37], [38] and Roberts *et al.* [39] have been doing continuous research

Manuscript received January 7, 2019; revised March 14, 2019; accepted June 9, 2019. Date of publication July 23, 2019; date of current version October 31, 2019. This work was supported in part by the Strategic Priority Research Program of the Chinese Academy of Sciences under Grant XDA19030101, in part by the National Key Research and Development Program of China under Grant 2017YFE0100800, in part by the National Natural Science Foundation of China under Grant 41871345, and in part by the International Partnership Program of the Chinese Academy of Sciences under Grant 131211KYSB20170046. *(Corresponding author: Fang Chen.)*

The authors are with the Key Laboratory of Digital Earth, Institute of Remote Sensing and Digital Earth, Chinese Academy of Sciences, Beijing 100101, China (e-mail: chenfang_group@radi.ac.cn).

Color versions of one or more of the figures in this article are available online at http://ieeexplore.ieee.org.

Digital Object Identifier 10.1109/TGRS.2019.2923248

TABLE I
S-VISSR INSTRUMENT CHANNELS

Channel No.	Spectral interval	SNR or NEΔT @ specified input	Spatial Resolution
1	10.3 - 11.3 μm	0.5 K @ 300 K	5 km
2	11.5 - 12.5 μm	0.5 K @ 300 K	5 km
3	6.30 - 7.60 μm	1.0 K @ 300 K	5 km
4	3.50 - 4.00 μm	0.5 K @ 300 K	5 km
5	0.55 - 0.99 μm	43 @ 95 % albedo	1.25 km (5 km) *

** Note:*
The 5th channel provides data with spatial resolution up to 1.25 km while it also provides resampled images with 5 km spatial resolution.
Independent cloud classification datasets are also stored as L1 data. Table 2 lists the meanings of the different cloud detection indexes (the 'CLD' dataset).

TABLE II
INTRODUCTION OF CLOUD DETECTION MASK

Index	Meaning
255	Invalid data
0	Water
1	Non-cloudy land
11-15	Cloud type I (Dense high cloud) [1]
21	Cloud type II (Non-dense high cloud) [2]
100	Margin (only partially exists)[3]

Note:
1. The index 11–15 was set for 'dense high clouds' and designated as 'Cloud type I'. Also, from the Figure 1, it could be seen that these cloud pixels affected the results more seriously and so these were not considered as valid pixels in this research.
2. The index 21 was set for 'non-dense high clouds' and designated as 'Cloud type II'. These pixels are affected by cloud although some fire pixels could still be detected by visual inspection.
3. The index 100 only partially exists on the margin of valid-data areas and is not described in the NSMC introduction files. Therefore, we named this index 'margin' in our research and pixels with index 100 were considered to be 'invalid data'.

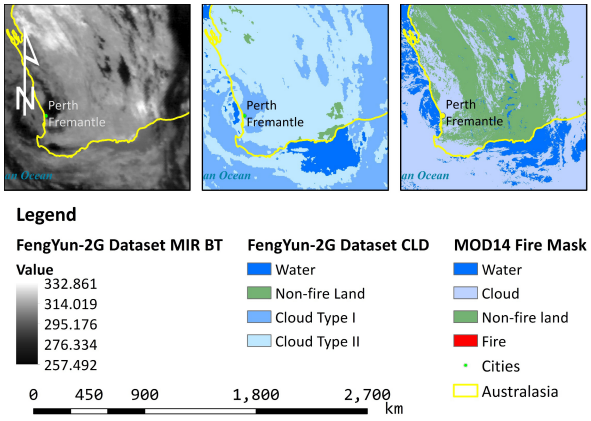

Fig. 1. Example of FY-2G S-VISSR mid-infrared channel values, cloud classification, and MODIS fire product results at 2:00 A.M. UTC on January 19, 2016.

on fire pixel detection using the Spinning Enhanced Visible and Infrared Imager (SEVIRI) and have achieved satisfactory results. Based on the achievements of earlier research, this study uses data from one of the Chinese geostationary satellites, FengYun-2G. Spatial analysis is included, and full use of the advantages of the high temporal resolution is made to detect and monitor active fires.

II. DATA SETS

The FengYun II (FY-2) meteorological satellites are the first generation of geostationary meteorological satellites developed by China independently and are designed to be complementary with the polar-orbiting meteorological satellites of the FY-1 and FY-3 series. The first geostationary meteorological satellite FY-2A was launched on June 10, 1997. FY-2G is the 5th operational satellite and the 2nd satellite in batch 3 of the FY-2 series. It is designed to obtain daytime visible cloud images, day and night infrared cloud and water vapor distribution maps, and to be a stable platform for collecting meteorological, hydrological, and marine data for domestic and foreign research. It was successfully launched on December 31, 2014, and is positioned at 105° E above the equator. Observation and data acquisition services began on June 3, 2015 [40]. Due to the position of FengYun-2G, it generally provides the imagery of East Asia, South Asia, Central Asia, and Oceania and provides data once every hour. Four extra images are acquired and offered at 5:30, 11:30, 17:30, and 23:30. The latest data sets have improved the temporal resolution to half an hour, which means users can be provided with 48 images per day. In this paper, to retain the same frequency of observations, the four extra images are abandoned.

FengYun-2G carries the Stretched Visible and Infrared Spin Scan Radiometer (S-VISSR), which contains five channels from the visible to the thermal infrared region. Details of these channels are shown below in Table I. The visible channel provides images at two different spatial resolutions. The 1.25-km resolution images (single band) are stored separately, while the 5-km resolution images are stored together with the images from the other channels. Channels 1, 4, and 5 were used in the algorithms. The channels are remarked as "TIR," "MIR," and "VIS," which represent thermal infrared, mid-infrared and visible channel, respectively. Besides, cloud classification has been stored in S-VISSR L1 data as well. Although the cloud masks are valid and effective, the results from cloud masks were too vague for algorithms to classify the cloud pixels accurately, which will increase the difficulty in selecting valid pixels in the following steps. As Fig. 1 shows, the CLD mask can portray the cloud pixels clearly comparing with MODIS result (MOD14A1). Nevertheless, more pixels are classified into cloud-affected pixels, namely, "Cloud Type II" in Table II. Excluding these pixels without distinction may cause obvious omission errors. Although the cloud classification was not utilized in this paper, the land and sea mask could be generated as a derivative by adding up a long series of CLD mask data.

Before the detection progress began, preprocessing of the data was required. The data was stored in S-VISSR L1 files in the form of discrete digital numbers (1–1024 for bands 1–4;

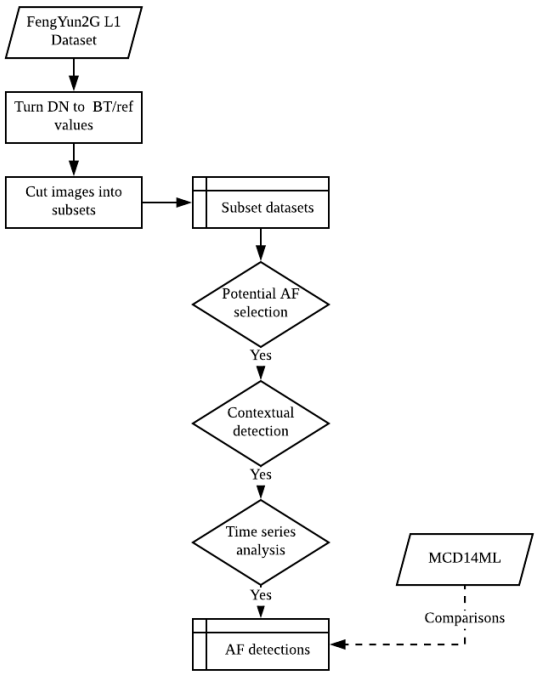

Fig. 2. Flowchart of the algorithm developed in this study. The algorithm generates binary classification results. (The AF within the boxes is the abbreviation for "active fire.")

1–64 for band 5) with no physical meanings. By checking look-up tables (LUTs) for corresponding channels, these DN (digital number) values will be turned into brightness temperature (BT) or reflectance values. Detailed descriptions of the involved scientific data sets and LUTs can be checked in Table III. Considering that the values for calibration have already been recorded in the LUTs, any pixels with even higher actual BT values could not be recognized correctly. According to the LUTs, the highest BT value for mid-infrared channel stored in the file is around 340 K.

III. Methodology

Although, already, there have been studies that have used geostationary satellite imagery, much of this previous research was based on the analysis of single-date imagery with pixels being detected as fire pixels using thresholding methods or other image processing methods [28], [31], [38]. Some other research was carried out based on time series analysis, while the image characteristics were not taken into consideration. However, a single S-VISSR image can provide only very limited information due to the relatively low spatial resolution. On the one hand, to better explore the potential of time-series analysis and take full advantage of the information contained in the imagery, temporal analysis is involved. On the other hand, the introduction of spatial analysis in this algorithm helps reduce the calculation time as well. By eliminating the pixels with obvious nonfire characterization, the calculation time will be saved, and the time series analysis will focus on some target areas. The flowchart of this algorithm has been shown in Fig. 2.

A. Data Preprocessing

In addition to the basic data processing, an image cropping is involved. The time series analysis procedures in fire detection algorithms are always the most time-consuming components. The processing of full disk images could be even slower without the high-performance instruments. For saving computation resources and computing time, image cropping would be involved in the data preprocessing step. The full disk image will be clipped into 169 (13×13) subsets. The size of each data set will be 176×176 pixels. Considering that the neighboring subsets may share connecting image information, a square ring with a size of 2 pixels will be added to every subset data set. The four sides of the 2-pixels-ring will contain different values based on the relative position among the 169 subsets. The sides, where there are also the outermost sides of the full disk image, would be filled in with value 0. On the other hand, the inner connected sides will be filled in with values from the neighboring data sets. By adding the neighboring values to every subset data set, the size will be changed to 180×180 pixels as well. Fig. 3 illustrates the full disk map and the selected subsets after image cropping. The horizontal and vertical labels can be utilized to identify the detailed images.

In this paper, two major research regions were selected, which generally cover parts of Southern Asia and the main area of Australia. The horizontal and vertical labels are listed as below. The red hollow circles in Fig. 4 show the fire pixels detected in January 2016, from MODIS products. A large number of fire pixels were located in the selected research areas. Besides, the FengYun-2G satellite is positioned at 105° E, where the data covering these areas would have relatively small geometric deformation.

B. Spatial Analysis

Spatial analysis is one of the common methods to calculate the characteristics of images and capture the anomalies, where fire pixels may locate. It can still be effective in the algorithms and variation in the infrared channels can be captured when the fire incidents take $10^{-3} \sim 10^{-4}$ of the pixels [39], [41]. Besides, by eliminating a large number of nonfire pixels, the computing resources can be saved as well for the upcoming time analysis step. In this paper, the spatial analysis procedure inherits and integrates the concepts of "potential fire tests" and "contextual tests" from [11], [12], [14], and [15]. Over 90% and 99% of the original pixels will be removed after these two steps. The "potential fire tests" will be applied to every pixel. Those that satisfy the requirements after the test will enter the "contextual tests." Values will be calculated further from the moving windows centered on the pixels, where the neighboring pixels can be sketched.

The potential fire tests contain the requirements concerning the multiple thresholds. The following are the detailed criteria:

$$T_{\mathrm{MIR}} \geq \overline{T_{\mathrm{MIR}}} + 5 \& T_{\mathrm{MIR}} \geq 310 \tag{1}$$

$$\Delta T \geq 15 \tag{2}$$

$$\mathrm{VIS} \leq 20 \tag{3}$$

where T_{MIR}, ΔT, and VIS represent MIR BT values, differences between MIR and TIR, and the reflectance of the visible channel. In the FengYun-2G data, MIR, TIR, and VIS values are acquired from channels IR4, IR1, and VIS, as Table III

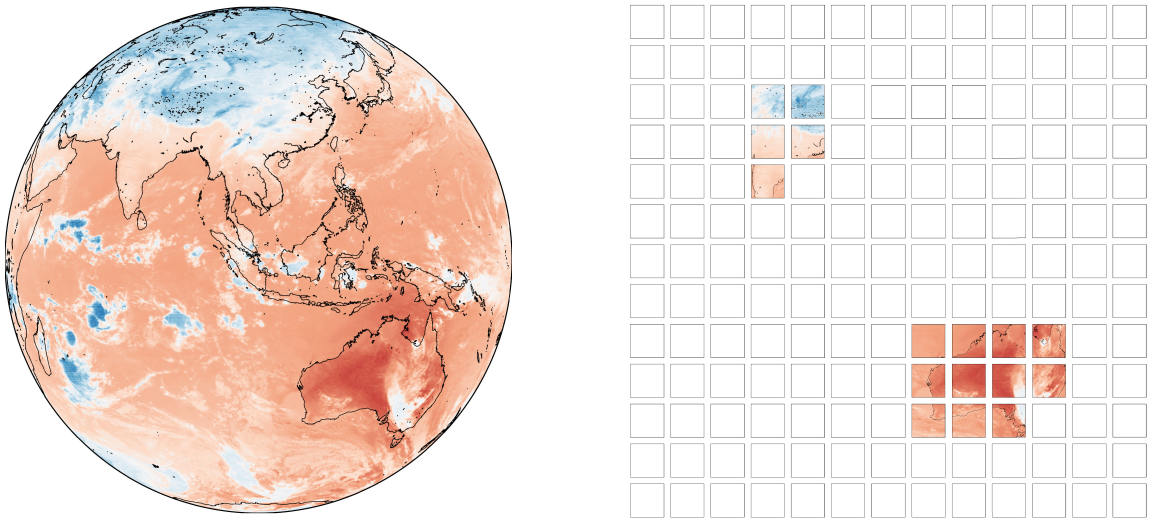

(a) (b)

Fig. 3. (a) Full disk image of FengYun-2G S-VISSR 4th channel captured at 0:00 A.M. UTC on January 1, 2016. The MIR BT values decrease as the color changes from red to blue. (b) Clusters of subsets clipped from full disk images. These subsets are selected as research areas.

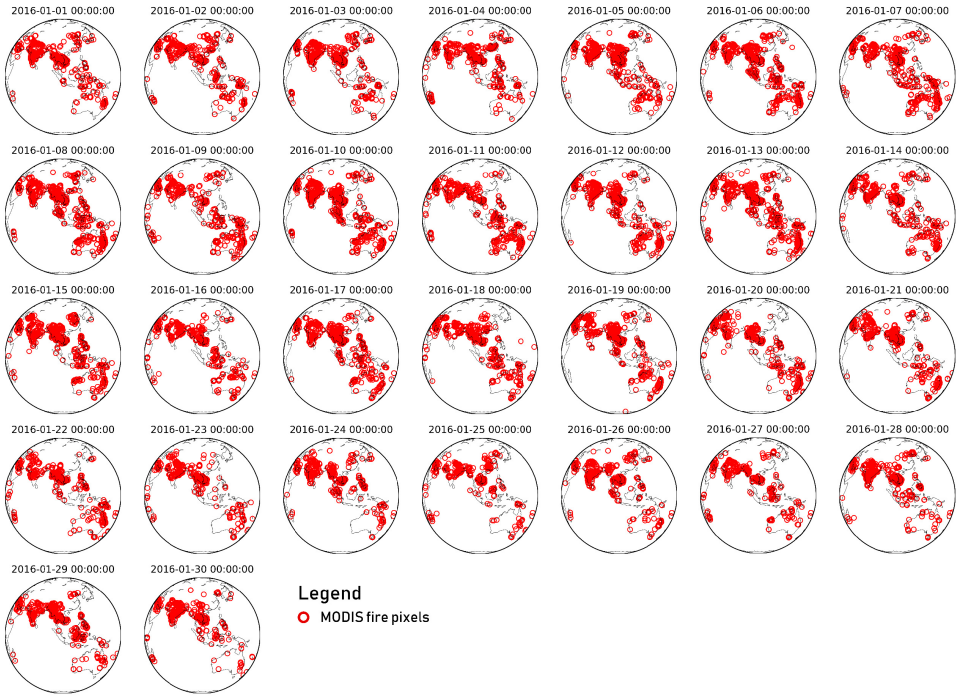

Fig. 4. Daily results of detected MODIS fire pixels on a monthly base. Each red hollow circle represents a fire pixel.

shows. $\overline{T_{\mathrm{MIR}}}$ is the average value of the subset images. Equation (1) contains both fixed and dynamic thresholds, where the fixed thresholds are defined based on [12], [15], and [42], and the dynamic thresholds are defined based on the statistical information of the images. Fig. 5 demonstrates the changes of one of the regions tested on January 7, 2016. The title for every subplot illustrates the imaging time and calculated values for the whole image. The BT values decrease as the colors change from red to blue on the heat maps. It is obvious to find that the characteristics of the images can vary a lot even in the same place at different times, such as the average MIR value. Therefore, a fixed lower limit is involved to expel pixels with obvious nonfire features, while the combining of dynamic thresholds will help to adapt to scenarios, where the fixed thresholds may not be effective. Fig. 6 shows the histograms of the MIR value from the corresponding subplots in Fig. 5. The percentages of pixels above two thresholds are listed in the title for every subplot. The solid and dashed vertical lines indicate the fixed and dynamic thresholds locations, respectively, in different places on the histograms. In the areas with low average MIR values, fixed thresholds keep the gate for rejecting most of the nonfire pixels which may contain pixels

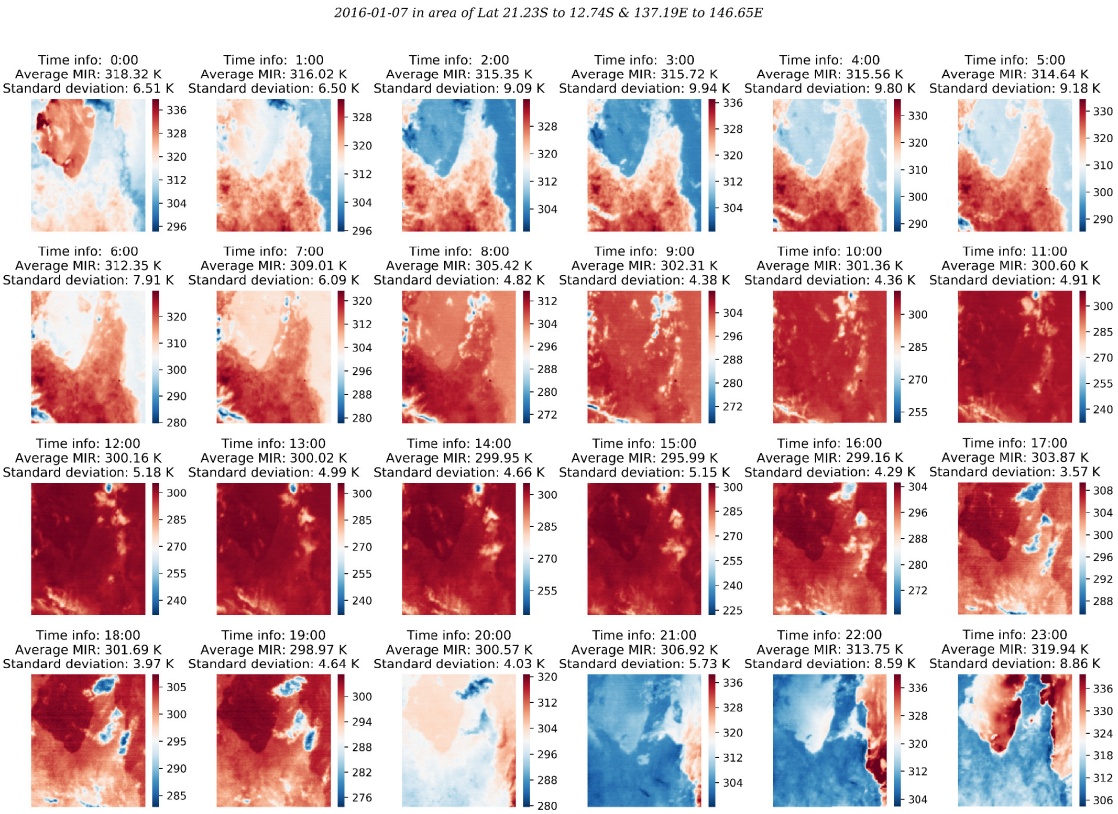

Fig. 5. Average and SD of MIR values within the 24 h of the region (H:10, V:08) on January 7, 2016. Values decrease as the color changes from red to blue.

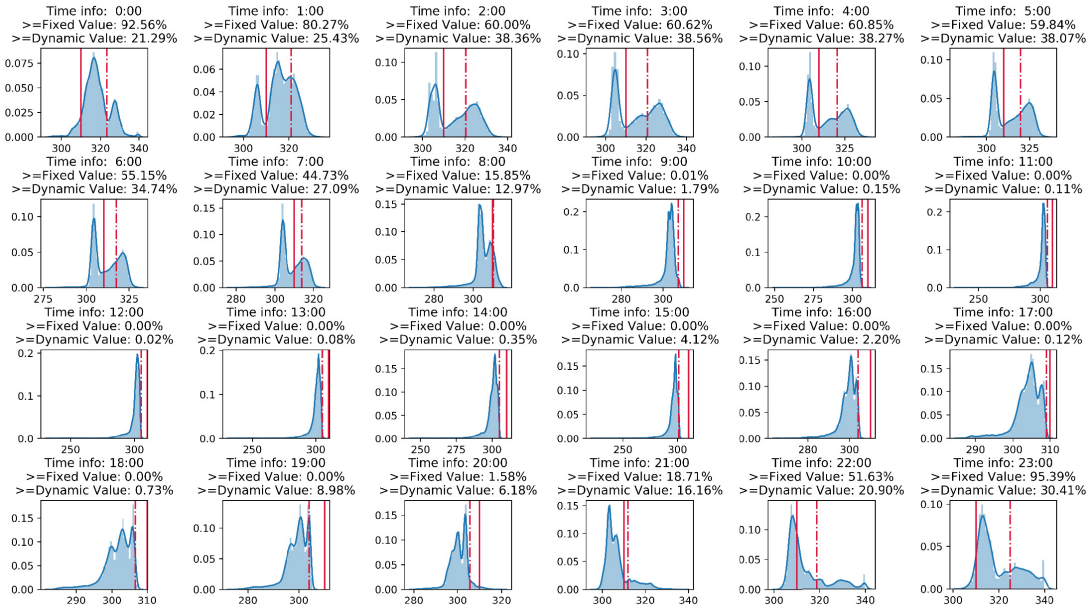

Fig. 6. Percentages of pixels with values above fixed and dynamic thresholds.

within the bright spots. In other cases, dynamic thresholds play the dominant role in eliminating extra yet unqualified pixels. Unlike the combination of dynamic and fixed thresholds, only fixed threshold 15 K is utilized in the potential fire tests. Pixels contaminated by clouds will have much stronger effects on the calculation of ΔT values and the fire pixels may be neglected.

Fig. 7 demonstrates the heat maps of ΔT values in different areas at different observation times. The average ΔT values can vary a lot when the percentage of cloud pixels change. The observation times of these areas are displayed in the subtitles. Indexes of the subset images are H3V4, H7V10, and H8V1, respectively, from the first to the third column. The average

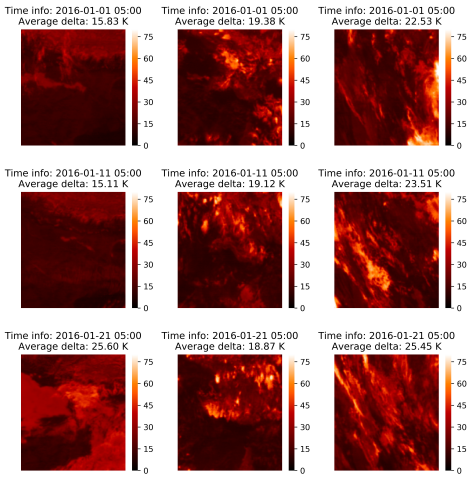

Fig. 7. Comparisons the average delta values among different areas at different times.

data can vary a lot, as Fig. 7 demonstrates. Equation (3) is set to remove the pixels with a high reflectance, such as the desert pixels or pixels on cloud edges, where the high reflectance is one of the main characteristics. The pixels which satisfy the above three requirements will enter the following contextual test. In addition to the above requirements, pixels within the water area will be rejected as nonfire pixels as well. Although the latest active fire detection algorithms have gained the ability in detecting the fire pixel in water areas [12], [43], it is still difficult to detect fire incidents on FengYun-2G images considering the low spatial resolution.

Contextual test contains the following several criteria:

$$T_{\mathrm{MIR}} \geq T'_{\mathrm{MIR,min}} + 15 \& \Delta T \geq \Delta T'_{\mathrm{min}} + 15 \tag{4}$$

$$T_{\mathrm{MIR}} \geq \overline{T'_{\mathrm{MIR}}} + 5 \& \Delta T \geq \overline{\Delta T} + 5 \tag{5}$$

$$T_{\mathrm{MIR}} \geq \overline{T'_{\mathrm{MIR}}} + 1.5 \& \overline{T'_{\mathrm{MIR}}} \geq 318 \& \Delta T \geq \overline{\Delta T} + 1. \tag{6}$$

The markers with superscripts illustrate the corresponding values calculated from the moving window with a window size of 2 pixels centered on the aim pixels. This size matches with the square ring added around the original subset data set as well. Equations (4)–(6) describe three parallel requirements designed from different scenarios. Equation (4) sets thresholds for comparisons based on the minimum values within the moving window, while (5) sets thresholds based on the average values. When pixels are in high MIR value regions, the variation may not be so obvious to detect comparison with the normal regions. Therefore, a lower dynamic MIR threshold is utilized. Pixels that meet any one of the above conditions will be added to the temporal analysis for further confirmation.

C. Temporal Analysis

One of the most important advantages of using geostationary satellites to detect active fire pixels is that, with the help of high temporal resolution images, the anomalies can be detected from minor changes. Besides, the multitemporal images can also draw the variations dynamically where the fire incidents can be monitored continuously. Research based on multitemporal active fire detection has been carried out continuously. One of the major achievements is to involve the method of modeling a diurnal temperature cycle (DTC). By modeling patterns of diurnal temperature changes, the values on aim images with confirmed observation time can be predicted. Active fires are outbreaks, which will cause BT values to rise in a short time and be far away from the normal states, namely the predicted values. Pixels can be detected when the observed value is high enough to reach the established requirements for temporal tests. To capture the pattern of temperature changes more precisely, various enhanced algorithms are involved to handle the abnormal data or outlier information.

Gottsche and Olesen [44] involved a robust estimator to enhance the performance and overcome the effects of remained cloud pixels. Roberts and Wooster [37] further explored the potentialities of DTC and established a mature system based on the robust matching algorithm [45] and the Kalman filter method [46]. This method can generate solid prediction results with low mean square errors based on previous observations even if there are large numbers of cloud-affected values. On the one side, the series of methods can make accurate assumptions to detect active fires. On the other side, the computing time limits the usage of these algorithms in larger areas or longer time series.

In this paper, a new aspect to analyze the variation of the pixels is introduced, where attentions are paid only to the values with the same observation time on different days. Fig. 8 shows the line charts of the changes, of a single pixel, within a month. The subplots demonstrated the daily changes with the same observation time during a whole month. The yellow lines are subsets of the blue lines, which record the valid data and original data series, respectively. The solid green lines indicate the average values calculated from the valid data series. As Fig. 8 shows, the differences among the values may be very large. Yet, there are certain fluctuation ranges around the average values indicating that every pixel changes within secure ranges if no sudden incidents occur. The ranges can be even clearer when invalid values are removed. The length of the time series is set to 30 days. Fig. 9 demonstrates the comparisons between the results generated from different lengths of the input data. Without any doubt, the calculation time increases as the length of input data grows and the trend tends to become smooth when the length is above 20. Alternatively, more errors can be avoided when there is more information to construct a time series. In addition, the systematical problems including omission of data from the archive, bad data quality, etc., should also be taken into consideration. Hence, we select 30 days as the length of the input time series data when the computation time is acceptable, and the insufficiencies of data will be avoided. The test shows that the average time for calculating every single pixel is around 1×10^{-4} s

$$T_{\mathrm{valid,ts}} = (T_{\mathrm{original,ts}} \geq 270) \tag{7}$$

$$T_{0.9999,\mathrm{top}} = \overline{T_{\mathrm{valid,ts}}} + t_{0.9999} * \frac{\sigma T_{\mathrm{valid,ts}}}{\sqrt{n}} \tag{8}$$

$$T_{\mathrm{MIR}} \geq T_{0.9999,\mathrm{top}} + 2 \tag{9}$$

$$T_{\mathrm{MIR}} \geq \max(T_{\mathrm{valid,ts}}) + 2.5. \tag{10}$$

TABLE III
DETAILED DESCRIPTION OF INVOLVED DATA SETS

Scientific datasets	Description	Dataset shape	Data type
CALIR1	Look-up table for IR1 channel calibration	[1 × 1024]	Float
CALIR2	Look-up table for IR2 channel calibration	[1 × 1024]	Float
CALIR3	Look-up table for IR3 channel calibration	[1 × 1024]	Float
CALIR4	Look-up table for IR4 channel calibration	[1 × 1024]	Float
CALVIS	Look-up table for VIS channel calibration	[1 × 64]	Float
NOMChannelIR1	IR1 Channel 5KM dataset	[2288 × 2288]	UINT16
NOMChannelIR2	IR2 Channel 5KM dataset	[2288 × 2288]	UINT16
NOMChannelIR3	IR3 Channel 5KM dataset	[2288 × 2288]	UINT16
NOMChannelIR4	IR4 Channel 5KM dataset	[2288 × 2288]	UINT16
NOMChannelVIS	VIS Channel 5KM dataset	[2288 × 2288]	UINT8
NOMCloudClassification	5KM Cloud classification results	[2288 × 2288]	UINT8

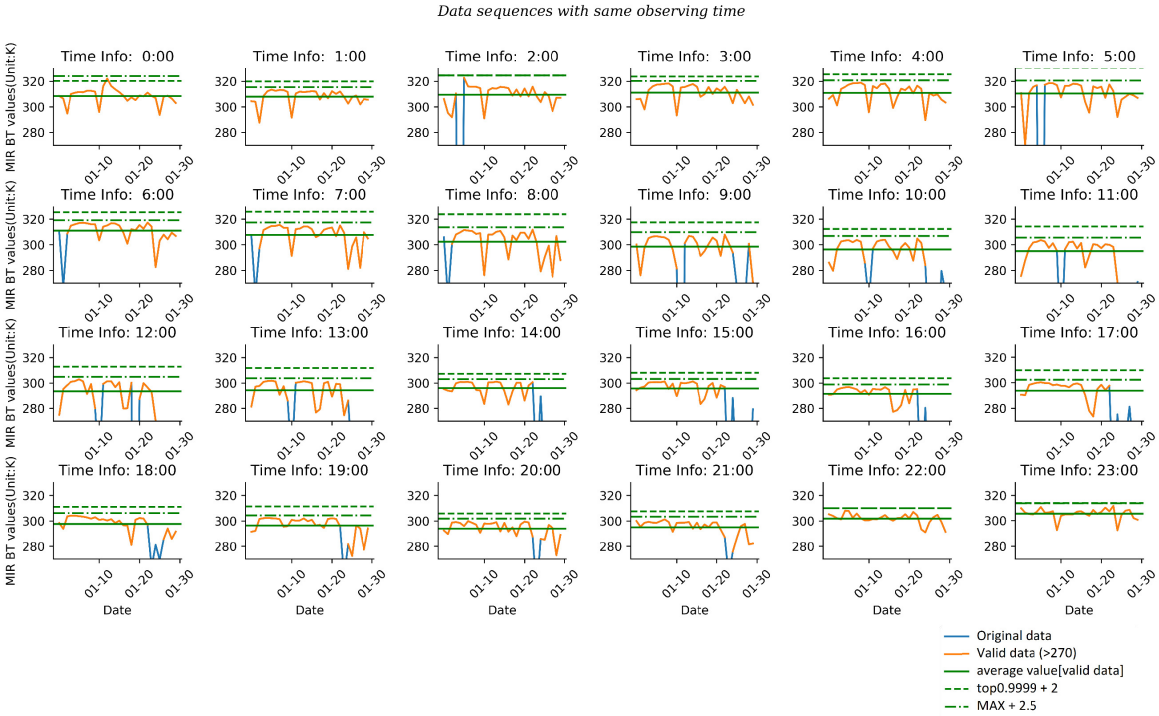

Fig. 8. Subplots of the daily changes where the titles illustrate the observing time. The meanings for different colors and lines are demonstrated as above. Two green dash/dotted-dash lines are the requirements in temporal analysis, respectively.

The $T_{\text{valid,ts}}$ and $T_{\text{original,ts}}$ denote the valid data sequences and original data sequences, respectively. Pixels that succeeded in tests in the spatial analysis will undertake the temporal analysis procedure. The original data contain values captured at the same observing time with a length of 30 days and valid data contain values above 270 K within the original series. The bad quality of data or part of cloud pixels may show the extreme low MIR values of the data. Besides, these values will strongly affect the calculation of the average and standard deviations (SD). Hence, only values above 270 K will be considered as valid. As mentioned above, the estimations of the fluctuation ranges would be made to depict the normal states of the pixels. For every pixel to be tested, since the observing time is set to be the same, the values are assumed to be within certain ranges. Fig. 10 gives several randomly selected pixels located at different places. The titles of subplots indicate the information including horizontal and vertical indexes of the subsets; x and y values of the map coordinates. The histograms are values of the time series of the pixels. Generally, the data sequences have the similar shapes of normal distribution. A total of 30 days' data was involved. Therefore, the knowledge of student's t-distribution can perform in this case. Thus, confidence intervals are introduced to draw the ranges where the pixel's value should be highly possible inside. Considering that the possibilities of fire incidents are rather low, we select an extremely high percentile value to conclude as many pixels as possible to avoid commission errors. In (8), the upper limit of the confidence interval, noted as $T_{0.9999,\text{top}}$, is calculated. $\overline{T_{\text{valid,ts}}}$ and $\sigma T_{\text{valid,ts}}$ are the average and SD values of the valid data within the sequence, while $t_{0.9999}$ is the t-score

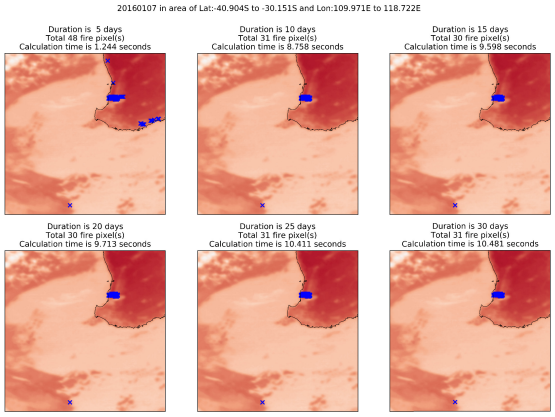

Fig. 9. Comparisons between the results generated from different lengths of time-series input data. The total amounts of detected fire pixels are listed in the titles for every subplot.

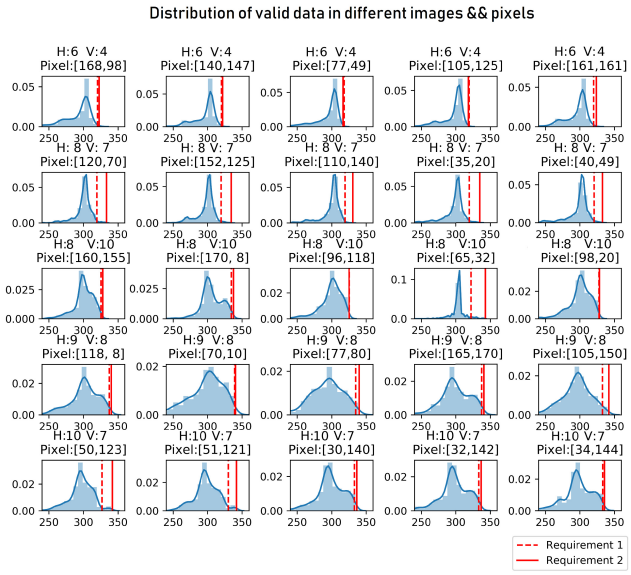

Fig. 10. Histograms demonstrating the distributions of valid data in different images and different pixels.

generated under the settings of the 99.99% percentile. $\sqrt{n}$ is the square root of the size of input data. Equations (9) and (10) introduce two separate and parallel criteria to test whether the pixel is beyond the thresholds. The 2 K is an empirical threshold set to validate that the increment between the pixel value and the upper limit is caused by abnormally high-temperature incidents rather than random disturbances. In some circumstances, the pixel value is higher than any other values within the sequences, while it is still less than the thresholds in (9). Equation (10) is set to make a supplementary judgement to decide if it is a fire pixel. A pixel that satisfies (9) or (10) will be considered as an outlier from the time series, namely, an active fire pixel.

IV. Results

It was necessary to assess the results of applying the algorithm to determine its advantages and shortcomings. In validation of active fire algorithms, the date and time of captured fire incidents from credible data sets should be concerned as well. Thus, the collection 6.1 Global Monthly Fire Location Product is introduced, namely MCD14ML. The monthly fire location product contains the geographic location, date, time, fire radiative power (FRP), detection confidence, etc. Every line stands for a detected single fire pixel by the Terra and Aqua MODIS sensors. For further systematical operations, the near-simultaneously recorded active fire detections products (MOD14 from Terra and MYD14 from Aqua), as well as the corresponding geolocation swath files (MOD03/MYD03), should be utilized.

Since the size of the FengYun-2G pixel is different from the MODIS pixel, we conduct the validation on a basis of virtual defined windows. For every FY-2G active fire pixel, a window with the same size of its pixel is predefined. It would be considered as true detection when there are more than one MODIS active fire pixel falling in the range of the window. The FY-2G pixels that fail to find any neighboring MODIS active fire pixels would be considered as commission errors. Similarly with the assessment of FY-2G pixels, a MODIS active fire pixel would be believed to be validated if it is found associated with an FY-2G pixel. Omission errors would occur when the pixel stands alone with no connections to any other FY-2G pixel. Furthermore, the time issue is an important factor in detecting active fire pixels. Therefore, the difference between the observing times is limited to less than an hour.

Generally, over 11 000 FengYun-2G subset images were selected in this paper. Results demonstrate the superiority of the geostationary data and this algorithm, as well as insufficiencies including multiple errors in detection. In the Australian regions, 3802 out of 6639 detect fire pixels were considered to be true detections, and 1827 out of 4090 MODIS active fires were detected with neighboring FengYun-2G detections. In the Indian regions, almost none of the MODIS active fires were detected, and only 127 detections were made by the algorithm. The following two cases indicate the results from MODIS fire products and this algorithm.

Fig. 11 illustrates one of the cases from the Australia research area. The results with fire pixels from MODIS products and this algorithm are superimposed together on the heat maps of FengYun-2G MIR channel. The values decrease as the color changes from red to blue. The series of images were captured on January 6 when bushfires took place in Yarloop, a historic mill town 110 km south of Perth. Fig. 12 shows that the fires lasted for a few days after the initial outbreaks according to the records of MODIS active fire products. The legend displays the fire pixels in different colors with the description indicating the name of the relevant files. The MODIS captured the initial separate traces of the fire incidents when the Terra satellite overpassed this area. The bushfire later expanded and seriously threatened the neighboring areas. Another MODIS image was taken within 17:00 to 18:00 UTC and few more fire pixels were captured. However, the increase of fire pixels in MODIS fire products is either not enough to reflect the seriousness of the bushfire or able to capture the dynamics. More fire pixels were detected on the results from MODIS fire products on January 7. Instead,

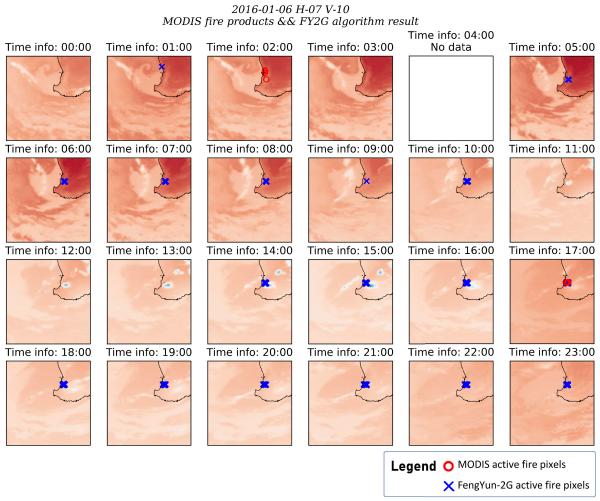

Fig. 11. Images of the detection results on one of the subsets. The solid lines indicate the southwest coast lines of Australia. Markers superimposed on the subplots are active fire pixels from MODIS products and FengYun-2G algorithms, respectively.

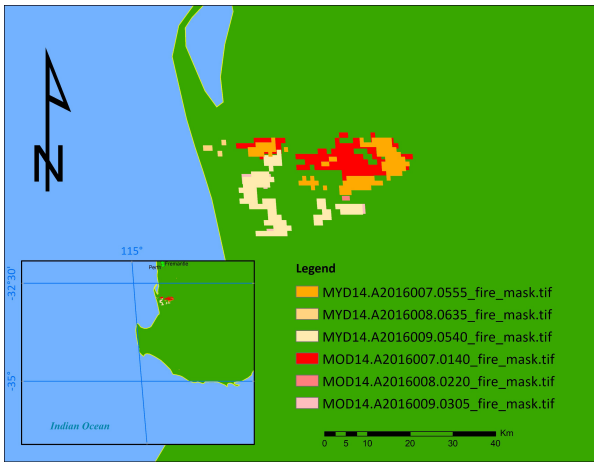

Fig. 12. Active fire detection captured from MODIS fire products.

hourly observations and the positioning on 105° E offer the ability to make continuous surveillance. As Fig. 11 shows, apart from the false detection at 2:00 UTC and lack of data at 4:00 UTC, the continuous detection began from 5:00 UTC. With more active fire pixels detected in the adjacent area and constant alarms, the smoke and plumes from the fire block the observation and no detections were made between 11:00 to 13:00 UTC. More continuous detections were made the next day, which was the same as the facts and results from MODIS products. FengYun-2G provides early-time fire detection and subsequent observations per hour to track the trends of the fires.

Although many of the FengYun results are validated to be true detection, both commission and omission errors are serious problems in the current result. In the three research regions, the dominant kinds of errors are different. Fig. 13 shows the detection results generated from MODIS fire product and FengYun-2G algorithm. The background images are similar heat maps of FengYun-2G MIR channel with the

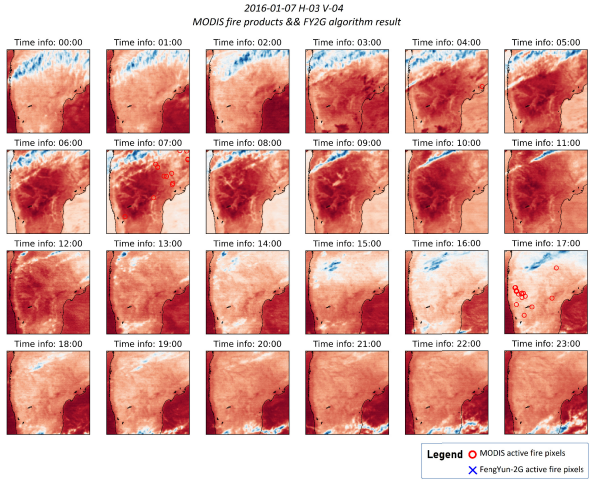

Fig. 13. Images of the detection results on one of the subsets. The solid lines indicate part of the west and east coast lines of the Indian subcontinent. Markers superimposed on the subplots are active fire pixels from MODIS products and FengYun-2G algorithms, respectively.

same color bar as that in Fig. 11. Sporadic active fire pixels were selected from MODIS fire products. The geolocation of these fire pixels distributed separately and few of them are connected to each other. In addition, the many pixels detected on 4:00 UTC were not further detected at 7:00 and 17:00 UTC. Thus, assumptions could be made that these pixels are detected from small fire incidents, which affected only neighboring areas and lasted short time periods. The FengYun-2G failed to make fire detections in this area. Small fire incidents should be the main reason for the obvious omission errors. To display and analyze the cause of these kinds of errors in the Indian research area, the detailed information at 17:00 UTC on the same day was selected from Fig. 13, where multiple MODIS fire pixels were detected. Fig. 14 shows the image at the mentioned time. Detailed knowledge for one of the FY-2G pixel was demonstrated in the subplots. The aimed pixel on FengYun-2G image is under fire incidents detected by MODIS fire products, while the pixel itself is not considered an active fire pixel by the algorithm. The subplot on the top illustrates the heat map of the neighboring area around the aimed pixel. The absolute value of the aimed pixel is not high enough to succeed in the spatial analysis, while the time series shows that the pixels are not higher than the required threshold either. Yet from the results of MODIS fire products, the pixel has an MIR value of 332.5 K of the observing time. Small fire incidents together with the ambient lower background temperature generate low MIR value in the mixed pixel.

Comparing cases of the fire pixels detected from FengYun-2G algorithm and MODIS fire products, we find that one of the major causes of these obvious omission errors is the sizes of the fire incidents. As confirmed on the figures superimposed with MODIS active fire products, the fire pixels are under a low detection rate when they scatter in different places. Therefore, to examine whether the distribution of the fire pixels had an influence on the accuracy of the algorithm, the sizes of the MODIS fire pixel polygons are calculated. Every polygon contains a single or a group of

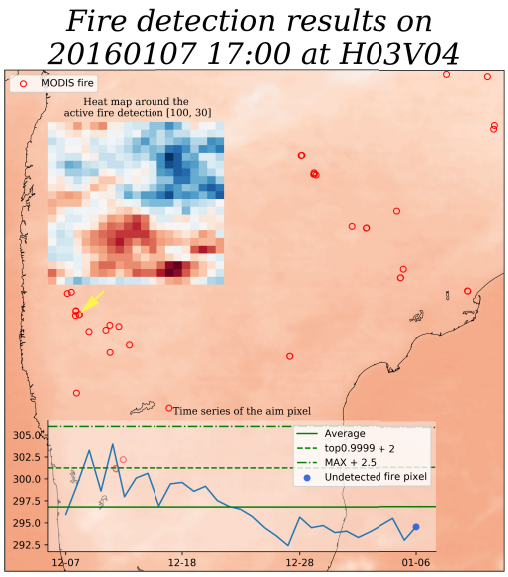

Fig. 14. Failure in detecting active fires in India research area.

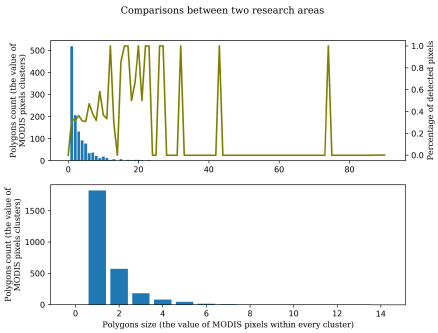

Fig. 15. Comparisons between two research areas in the count of fire polygons.

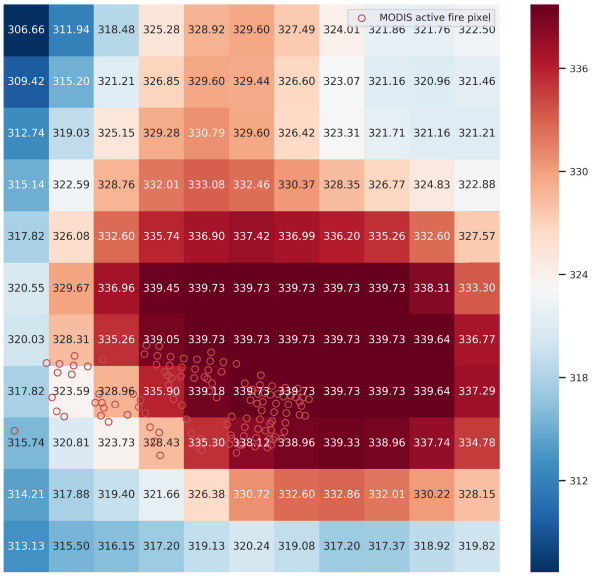

Fig. 16. Heat map of FengYun-2G MIR data with MODIS active fire products superimposed on.

spatial contiguous fire pixels. Both the number of fire pixel polygons and the fire pixels within the polygons are calculated. Fig. 15 shows the comparisons between the two research areas in the count of fire polygons. The x-axis in every subplot shows the number of fire pixels within a single polygon, while the y-axis is the number of corresponding polygons. The percentage of true detection polygons are plotted on the first subplot as well, which can justify the fact that the algorithm works better in larger sizes of fire incidents. According to the results, the average size of fire incidents in Australia contains 3.39 MODIS fire pixels while the size in India is 1.59 MODIS fire pixels. From the aspect of FengYun-2G detection results, the same conclusion could be drawn. In the Australian research area, an average of 18.62 MODIS fire pixels is contained within the window of FengYun-2G as described in the validation part. Fig. 16 demonstrated a heat map centered on an active fire from FengYun-2G data. The map shows the neighboring area with the pixels' MIR values marked inside. MODIS active fire pixels within this area are marked in red hollow circles. It is obvious that under the circumstances, where the more MODIS active fire pixels are gathering, the more omission errors would be avoided.

V. Discussion and Conclusion

This paper has described an active fire-detection algorithm for use with data acquired by the Chinese geostationary satellite, FengYun-2G. Numerous active fire-detection algorithms have been developed in the past, but only a few of them are designed for geostationary data and even fewer for Chinese satellite data. FengYun-2G is an operational satellite and provides researchers with 5-km spatial resolution data every hour. As the spatial analysis method helps in removing many of the unrelated pixels, the high temporal resolution and time series analysis assist in characterizing pixels and avoiding mistakes caused by coarse spatial resolution. Fully developing the potentialities of time-series analysis becomes essential. The proposed algorithm consists of three major steps: data preprocessing, spatial analysis, and temporal analysis. A universal method for processing full-disk images is introduced and would greatly enhance the efficiency of further calculation especially in research, where the emphasis may be concentrated on certain local areas. During the spatial analysis, potential fire tests are utilized with the support of a combination of fixed and dynamic thresholds to eliminate nonfire pixels to the max extent. The coming contextual tests further help to narrow down the range of pixels. Subsequently, a time series analysis method is introduced where data sequences with the same observing time are taken as input data. Different from previous research where people tried to simulate the patterns of the BT values of diurnal changes, the solid fluctuation ranges are the core contents to capture. For every pixel to be tested, the input data were analyzed based on the knowledge of students' t-distribution. Thus, confidence intervals with high percentile number are constructed. Active fire detections are made according to the calculated confidence intervals and the max value from the input data sequence. The algorithm works stable and fast. However, the results still have serious problems to be fixed. Obvious errors, especially omission errors, are a serious problem as is also the case with other geostationary algorithms.

The research for geostationary has been performed for decades while few algorithms were designed for FengYun-2G algorithm. This paper sketched an active fire detection algorithm based on the previous study of contextual and temporal analysis methods. But the evident insufficiencies remind us that further developments should be made. One of the future research directions is to drop the error rate by adding false alarm elimination schemes and enhancing the ability to capture small fire incidents. Another direction is to involve multiple sources of data, which is under research currently. The data include those from polar-orbiting satellites, which can provide higher spatial resolution and new geostationary satellite. With the sequence of FY3 series data now in operation, more information about the same research area with different data can help to draw the characteristics more accurately. New data sets are available from the China Meteorological Administration as well. The new Chinese geostationary satellite FengYun-4A was launched on December 10, 2016 and carries newly designed instruments including the Lightning Mapping Imager (LMI) and the Advanced Geostationary Radiation Imager (AGRI). The AGRI instrument provides 14 channels with spectral bands including the visible, infrared, shortwave infrared, mid-infrared, and thermal infrared. The spatial resolution has been upgraded to 0.5–4 km depending on the channel and the temporal resolution has been upgraded to 15 min. All these upgrades strengthen the ability to carry out active fire detection and continuous monitoring. In addition, another satellite in the FengYun-2 series, FengYun-2H has now been in service with the same instrument S-VISSR on board, which makes the algorithm to function for FengYun-2H data as well. In the future, new algorithms could be constructed based on the new FengYun-4 satellite data. More concentrations would be placed on various upgraded instruments to enhance the performance of the algorithms. Finally, the study areas will be expanded to cover more than just Australia. The research contents will be expanded to include the energy of burning pixels rather than merely the detection. This will help to quantify the limitations of fire detection by using the S-VIRRS data.

This work has further explored the ability of FY-2G, a Chinese satellite, to carry out active fire detection. This study was based on previous research using both polar-orbiting and geostationary data and used spatial as well as temporal analysis. Although the calculation speed met the necessary requirements for processing time series data, the error rate was still comparatively high, which means that there is still a lot of room for improving the algorithm. Among the problems to fix, omission errors should be the first. Further development of the algorithm and the use of next-generation satellite data should allow a more accurate and faster algorithm to be developed in the future.

REFERENCES

[1] S. H. Doerr and C. Santín, "Global trends in wildfire and its impacts: Perceptions versus realities in a changing world," *Philos. Trans. Royal Soc. B, Biol. Sci.*, vol. 371, no. 1696, 2016, Art. no. e0345.

[2] R. E. Keane *et al.*, "Ecological effects of large fires on US landscapes: Benefit or catastrophe?" *Int. J. Wildland Fire*, vol. 17, pp. 696–712, Dec. 2008.

[3] N. Preece, "Traditional and ecological fires and effects of bushfire laws in north Australian savannas," *Int. J. Wildland Fire*, vol. 16, pp. 378–389, Aug. 2007.

[4] W. Knorr, A. Arneth, and L. Jiang, "Demographic controls of future global fire risk," *Nature Climate Change*, vol. 6, pp. 781–785, May 2016.

[5] E. Chuvieco, L. Giglio, and C. Justice, "Global characterization of fire activity: Toward defining fire regimes from Earth observation data," *Global Change Biol.*, vol. 14, pp. 1488–1502, Jul. 2008.

[6] F. Mouillot and C. B. Field, "Fire history and the global carbon budget: A 1 degrees × 1 degrees fire history reconstruction for the 20th century," *Global Change Biol.*, vol. 11, no. 3, pp. 398–420, 2005.

[7] M. Matson and J. Dozier, "Identification of subresolution high temperature sources using a thermal IR sensor," *Photogramm. Eng. Remote Sens.*, vol. 47, no. 9, pp. 1311–1318, 1981.

[8] J. Dozier, "A method for satellite identification of surface temperature fields of subpixel resolution," *Remote Sens. Environ.*, vol. 11, pp. 221–229, Jan. 1981.

[9] M. D. Flannigan and T. H. V. Haar, "Forest fire monitoring using NOAA satellite AVHRR," *Can. J. Forest Res.*, vol. 16, no. 5, pp. 975–982, 1986.

[10] T. F. Lee and P. M. Tag, "Improved detection of hotspots using the AVHRR 3.7-um channel," *Bull. Amer. Meteorol. Soc.*, vol. 71, no. 12, pp. 1722–1730, Dec. 1990.

[11] L. Giglio, J. Descloitres, C. O. Justice, and Y. J. Kaufman, "An enhanced contextual fire detection algorithm for MODIS," *Remote Sens. Environ.*, vol. 87, pp. 273–282, Oct. 2003.

[12] L. Giglio, W. Schroeder, and C. O. Justice, "The collection 6 MODIS active fire detection algorithm and fire products," *Remote Sens. Environ.*, vol. 178, pp. 31–41, Jun. 2016.

[13] I. Csiszar *et al.*, "Active fires from the Suomi NPP visible infrared imaging radiometer suite: Product status and first evaluation results," *J. Geophys. Res.*, vol. 119, no. 2, pp. 803–816, 2014.

[14] W. Schroeder, P. Oliva, L. Giglio, and I. A. Csiszar, "The New VIIRS 375 m active fire detection data product: Algorithm description and initial assessment," *Remote Sens. Environ.*, vol. 143, pp. 85–96, Mar. 2014.

[15] Z. Lin *et al.*, "FengYun-3C VIRR active fire monitoring: Algorithm description and initial assessment using MODIS and landsat data," *IEEE Trans. Geosci. Remote Sens.*, vol. 55, no. 11, pp. 6420–6430, Nov. 2017.

[16] L. He and Z. Li, "Enhancement of a fire detection algorithm by eliminating solar reflection in the mid-IR band: Application to AVHRR data," *Int. J. Remote Sens.*, vol. 33, pp. 7047–7059, May 2012.

[17] R. S. Gautam, D. Singh, and A. Mittal, "An efficient contextual algorithm to detect subsurface fires with NOAA/AVHRR data," *IEEE Trans. Geosci. Remote Sens.*, vol. 46, no. 7, pp. 2005–2015, Jul. 2008.

[18] K. A. Kalpoma and J.-I. Kudoh, "A new algorithm for forest fire detection method with statistical analysis using NOAA AVHRR images," *Int. J. Remote Sens.*, vol. 27, no. 18, pp. 3867–3880, 2006.

[19] A. Abuelgasim and R. Fraser, "Day and night-time active fire detection over North America using NOAA-16 AVHRR data," in *Proc. IEEE Int. Geosci. Remote Sens. Symp.*, Jun. 2002, pp. 1489–1491.

[20] P. M. Barbosa, J.-M. Grégoire, and J. M. C. Pereira, "An algorithm for extracting burned areas from time series of AVHRR GAC data applied at a continental scale," *Remote Sens. Environ.*, vol. 69, pp. 253–263, Sep. 1999.

[21] M. Nakayama, M. Maki, C. D. Elvidge, and S. C. Liew, "Contextual algorithm adapted for NOAA-AVHRR fire detection in Indonesia," *Int. J. Remote Sens.*, vol. 20, no. 17, pp. 3415–3421, 1999.

[22] L. He and Z. Li, "Enhancement of a fire-detection algorithm by eliminating solar contamination effects and atmospheric path radiance: Application to MODIS data," *Int. J. Remote Sens.*, vol. 32, pp. 6273–6293, Aug. 2011.

[23] T. R. K. Chand, K. V. S. Badarinath, M. S. R. Murthy, G. Rajshekhar, C. D. Elvidge, and B. T. Tuttle, "Active forest fire monitoring in Uttaranchal State, India using multi-temporal DMSP-OLS and MODIS data," *Int. J. Remote Sens.*, vol. 28, no. 10, pp. 2123–2132, 2007.

[24] Y. J. Kaufman *et al.*, "Potential global fire monitoring from EOS-MODIS," *J. Geophys. Res.*, vol. 103, no. 24, pp. 32215–32238, 1998.

[25] W. Schroeder, P. Oliva, L. Giglio, B. Quayle, E. Lorenz, and F. Morelli, "Active fire detection using Landsat-8/OLI data," *Remote Sens. Environ.*, vol. 185, pp. 210–220, Nov. 2016.

[26] A. Koltunov, S. L. Ustin, B. Quayle, B. Schwind, V. G. Ambrosia, and W. Li, "The development and first validation of the GOES Early Fire Detection (GOES-EFD) algorithm," *Remote Sens. Environ.*, vol. 184, pp. 436–453, Oct. 2016.

[27] C. H. Wickramasinghe, S. Jones, K. Reinke, and L. Wallace, "Development of a multi-spatial resolution approach to the surveillance of active fire lines using Himawari-8," *Remote Sens.*, vol. 8, p. 932, Nov. 2016.

[28] M. J. Wooster *et al.*, "LSA SAF Meteosat FRP products–Part 1: Algorithms, product," *Atmos. Chem. Phys.*, vol. 15, no. 22, pp. 13217–13239, 2015.

[29] G. Kim, D.-S. Kim, K.-W. Park, J. Cho, K.-S. Han, and Y.-W. Lee, "Detecting wildfires with the Korean geostationary meteorological satellite," *Remote Sens. Lett.*, vol. 5, pp. 19–26, Jan. 2014.

[30] N. I. Sifakis, C. Iossifidis, C. Kontoes, and I. Keramitsoglou, "Wildfire detection and tracking over greece using MSG-SEVIRI satellite data," *Remote Sens.*, vol. 3, pp. 524–538, Mar. 2011.

[31] W. Xu, M. J. Wooster, G. Roberts, and P. Freeborn, "New GOES imager algorithms for cloud and active fire detection and fire radiative power assessment across North, South and Central America," *Remote Sens. Environ.*, vol. 114, pp. 1876–1895, Sep. 2010.

[32] S. D. Miller, G. L. Stephens, and R. T. Austin, "GOES 10 cloud optical property retrievals in the context of vertically varying microphysics," *J. Geophys. Res. Atmos.*, vol. 106, pp. 17981–17995, Aug. 2001.

[33] E. M. Prins, J. M. Feltz, W. P. Menzel, and D. E. Ward, "An overview of GOES-8 diurnal fire and smoke results for SCAR-B and 1995 fire season in South America," *J. Geophys. Res. Atmos.*, vol. 103, no. 24, pp. 31821–31835, 1998.

[34] J. F. Weaver, D. Lindsey, D. Bikos, C. C. Schmidt, and E. Prins, "Fire detection using GOES rapid scan imagery," *Weather Forecasting*, vol. 19, no. 3, pp. 496–510, 2004.

[35] M. Amraoui, C. C. DaCamara, and J. M. C. Pereira, "Detection and monitoring of African vegetation fires using MSG-SEVIRI imagery," *Remote Sens. Environ.*, vol. 114, pp. 1038–1052, May 2010.

[36] E. M. Prins and W. P. Menzel, "Geostationary satellite detection of bio mass burning in South America," *Int. J. Remote Sens.*, vol. 13, no. 15, pp. 2783–2799, 1992.

[37] G. Roberts and M. J. Wooster, "Development of a multi-temporal Kalman filter approach to geostationary active fire detection fire radiative power (FRP) estimation," *Remote Sens. Environ.*, vol. 152, pp. 392–412, Sep. 2014.

[38] G. J. Roberts and M. J. Wooster, "Fire detection and fire characterization over Africa using Meteosat SEVIRI," *IEEE Trans. Geosci. Remote Sens.*, vol. 46, no. 4, pp. 1200–1218, Apr. 2008.

[39] G. Roberts, M. J. Wooster, G. L. W. Perry, N. Drake, L.-M. Rebelo, and F. Dipotso, "Retrieval of biomass combustion rates and totals from fire radiative power observations: Application to southern Africa using geostationary SEVIRI imagery," *J. Geophys. Res. Atmos.*, vol. 110, pp. 1–20, Nov. 2005.

[40] National Satellite Meteorological Center. (2017). *Satellite Details of FengYun-2G*. Available:. [Online]. Available: http://www.nsmc.org.cn/en/NSMC/Channels/FY_2G.html

[41] M. J. Wooster, G. Roberts, G. L. W. Perry, and Y. J. Kaufman, "Retrieval of biomass combustion rates and totals from fire radiative power observations: FRP derivation and calibration relationships between biomass consumption and fire radiative energy release," *J. Geophys. Res. Atmos.*, vol. 110, Dec. 2005, Art. no. D24311.

[42] T. N. Polivka, J. Wang, L. T. Ellison, E. J. Hyer, and C. M. Ichoku, "Improving nocturnal fire detection with the VIIRS day–night band," *IEEE Trans. Geosci. Remote Sens.*, vol. 54, no. 9, pp. 5503–5519, Sep. 2016.

[43] Z. Lin *et al.*, "An active fire detection algorithm based on multi-temporal FengYun-3C VIRR data," *Remote Sens. Environ.*, vol. 211, pp. 376–387, Jun. 2018.

[44] F. M. Göttsche and F. S. Olesen, "Modelling of diurnal cycles of brightness temperature extracted from METEOSAT data," *Remote Sens. Environ.*, vol. 76, no. 3, pp. 337–348, Jun. 2001.

[45] M. J. Black and A. D. Jepson, "EigenTracking: Robust matching and tracking of articulated objects using a view-based representation," *Int. J. Comput. Vis.*, vol. 26, no. 1, pp. 63–84, 1998.

[46] R. E. Kalman, "A new approach to linear filtering and prediction problems," *J. Basic Eng.*, vol. 82, pp. 35–45, Mar. 1960.

Zhengyang Lin received the B.S. degree in cartography and geographical information system from Tianjin Normal University, Tianjin, China, in 2014. He is currently pursuing the Ph.D. degree in cartography and geography information system with the Institute of Remote Sensing and Digital Earth, Chinese Academy of Sciences, Beijing, China.

His research interests include active fire detection by using Chinese Fengyun satellites, and burned area and increase the accuracy of active fire detection with coarse resolution remote sensing images.

Fang Chen received the B.Sc. degree in science of environment from Northwestern Polytechnical University, Xi'an, China, in 2003, and the Ph.D. degree in cartography and geographic information system from the Institute of Remote Sensing Applications, Chinese Academy of Sciences (CAS), Beijing, China, in 2007.

He is currently a Professor with the Institute of Remote Sensing and Digital Earth, CAS. He conducts interdisciplinary work combining, remote sensing, ecology, and other fields of study to assess spatial patterns of disaster risk. He is an expert on wildfire, employing satellite remote sensing to assess the characteristics, behavior, and severe effects of fire in semi-arid rangeland and temperate forests that are inherent to current systems of human land-use and management. He has completed numerous research projects since he started his academic career and is a blossoming scholar who has a splendid record publication. He has authored over 30 original research articles in peer-reviewed, internationally recognized journals and holds one patent.

Dr. Chen has been involved in numerous professional activities and speaks worldwide on a broad range of earth observation and disaster issues. In 2011, he was elected to the CAS "Hundred Talent Program" and he is currently serving as the Executive Deputy Director of the CAS-TWAS Centre of Excellence on Space Technology for Disaster Mitigation (SDIM), coordinating and involving in multiple collaborative projects related to capacity building in disaster risk management in developing countries. He was selected as a TWAS Young Affiliate Fellow in 2014.

Bin Li received the B.S. degree in cartography and geographical information system from the China University of Mining and Technology, Xuzhou, China, in 2004, and the M.S. degree in cartography and geographical information system and the Ph.D. degree from the Chinese Academy of Sciences (CAS), Beijing, China, in 2007 and 2010, respectively.

He is currently an Associate Professor of GIS and remote sensing science with the Institute of Remote Sensing and Digital Earth, CAS. He has authored more than 20 papers in related journals. His research interests include the theory and application of spatial and temporal data mining.

Dr. Li is a member of the International Society for Digital Earth (ISDE).

Bo Yu is currently an Associate Professor of environmental disasters with the Institute of Remote Sensing and Digital Earth, Chinese Academy of Sciences, Beijing, China. She has joined three programs about applications of high spatial resolution images in hazard evaluation system and key techniques in investment program detection. Her research interests include climate change, fire detection, constructions detection, remote sensed images processing algorithms, machine learning, and time-series analysis.

Huicong Jia received the Doctoral Degree from Beijing Normal University, Beijing, China, in 2010.

She is currently an Associate Professor with the Institute of Remote Sensing and Digital Earth, Chinese Academy of Sciences, Beijing. Her research interests include the application of RS/GIS technology in drought disaster and risk analysis and disaster management via geospatial technologies.

Meimei Zhang received the B.S. and M.S. degrees in cartography and geographic information sciences from China Agricultural University, Beijing, China, in 2012, and the Ph.D. degree from the Institute of Remote Sensing and Digital Earth, Chinese Academy of Sciences (CAS), Beijing, in 2016.

She is currently an Assistant Researcher with the Institute of Remote Sensing and Digital Earth, CAS. Her research interests include the retrieval of disaster characteristic parameters and its application.

Dong Liang received the B.Sc. degree in applied mathematics from the University of Hull, Hull, U.K., in 2006, and the M.Sc. degree in applied mathematics from Mälardalen University, Västerås, Sweden, in 2009. He is currently pursuing the Ph.D. degree in cartography and geography information system with the University of Chinese Academy of Sciences, Beijing, China.

His research interests include big earth data.